Oxidation of Metals (2019) 91:495–510
https://doi.org/10.1007/s11085-019-09895-0

ORIGINAL PAPER

Effect of Nanostructured Surface on the Corrosion Behavior of RAFM Steels

Yanhong Lu[1] · Maolong Zhang[1] · Weibao Tang[1] · Yuanyuan Song[2] · Lijian Rong[2]

Received: 8 May 2018 / Published online: 24 January 2019
© Springer Science+Business Media, LLC, part of Springer Nature 2019

Abstract

This study investigated the effect of a preformed nanostructured surface on the corrosion behavior of 9Cr2WVTa reduced activation ferritic/martensitic (RAFM) steel and 9Cr+AlSi steel (9Cr2WVTa with the 0.12 wt.% Al and 0.68 wt.% Si addition) at 700 °C in air and at 550 °C in liquid lead–bismuth eutectic (LBE) alloys. The nanostructured surface layer was fabricated by surface mechanical rolling treatment (SMRT). The results showed that the SMRT 9Cr+AlSi sample has a lower oxidation rate than the SMRT 9Cr2WVTa steel at 700 °C in air, due to the faster diffusion rates of Al, Cr and Si in the nanostructure and a higher diffusion driving force increased by Cr. The SMRT 9Cr+AlSi sample at 550 °C in oxygen-saturated LBE alloy also had a higher oxidation rate, due to the formation of Al and Si oxides in the internal oxide layer.

Graphical Abstract

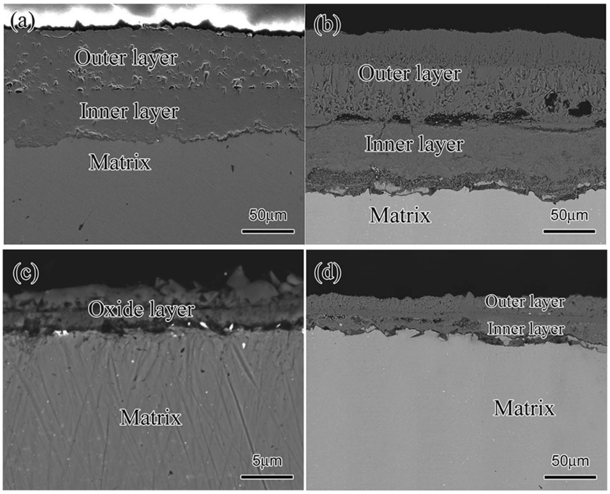

Extended author information available on the last page of the article

Keywords Nanostructured surface · RAFM · Corrosion · LBE alloy

Introduction

Reduced activation ferritic/martensitic (RAFM) steels with 9–12% Cr are the primary candidate alloys for the first wall and blanket structures of future accelerator-driven systems (ADS) and fission and fusion energy systems [1, 2] because of their inherent void swelling resistance coupled with low thermal expansion coefficient and high thermal conductivity compared with austenitic steels [3–5]. Irradiation embrittlement is associated with the alloying elements Mo, Ni and Nb in commercial martensitic steels which are able to be replaced by W, V and Ta [6–9]. RAFM steels show good thermophysical and mechanical properties, especially low sensitivity to radiation-induced swelling and helium embrittlement under neutron irradiation [1]. Variant of this steel has been developed in many countries, such as 9Cr2WVTa steels in USA [10] and the Chinese low activation martensitic steel (CLAM) [11]. Since the RAFM steels are serviced at 550–600 °C or higher, their mechanical property and oxidation resistance at higher temperature need concerns. Dunning et al. [12] investigated the effect of Si and Al additions on the oxidation resistance of austenitic stainless steels. The results showed that weight gains of the alloys containing these additions were half of the conventional alloy Fe-16Cr-16Ni-2Mn-1Mo in air at 700 °C and 800 °C. The steam oxidation rate of 9Cr–0.5Mo–1.8 W steel at 700 °C has been shown to decrease with increasing silicon content [13]. Further, the oxidation resistance of nanocrystalline 304 stainless steel at high temperature is much better than that of conventional polycrystalline counterpart [14].

In this work, the effects of a preformed nanostructured surface layer and the addition of 0.12 wt.% Al and 0.68 wt.% Si on the oxidation of 9Cr2WVTa at 700 °C in air and at 550 °C in lead–bismuth eutectic (LBE) alloy were studied. It was found that Al and Si addition improves the oxidation resistance of 9Cr2WVTa in air and in liquid LBE alloy effectively. The mechanism is also discussed.

Experimental Procedures

Sample Preparation

The measured chemical compositions of the 9Cr2WVTa and 9Cr+AlSi steels studied are given in Table 1. The initial material was hot-forged, water quenched after

Table 1 Chemical compositions of the 9Cr2WVTa and 9Cr+AlSi RAFM steel (in wt.%)

	C	Cr	W	V	Ta	Mn	Si	Al	Fe
9Cr2WVTa	0.104	8.61	1.66	0.25	0.08	0.49	< 0.10	< 0.05	Balance
9Cr+AlSi	0.16	9.01	1.92	0.25	0.12	0.61	0.68	0.12	Balance

austenitization at 1050 °C for 1 h and finally tempered at 750 °C for 2 h. The tempered microstructure consists of lath martensite and $M_{23}C_6$ which precipitates along the lath and prior austenite grain boundaries [15]. Rod samples were cut from the billet and subjected to SMRT. A detailed description of the SMRT setup and procedure has been described elsewhere [15], and the same process parameters were used in this study.

Oxidation Tests in Air and in Liquid LBE Alloy

Arc-shaped samples were cut from the cylindrical rod by using the electrospark discharge method, with an arc height of 3 mm, a width of 10 mm and a length of 14 mm. The surface was carefully ground to a 2000-grit finish using SiC abrasive papers, polished using diamond paste and then degreased in acetone and finally dried. Isothermal oxidation tests of the arc samples in static air were carried out at 700 °C for different durations for up to 500 h. All the samples were placed in a dry crucible in order to avoid weight loss by spallation. After testing, samples were removed from the furnace, air-cooled and then weighed at room temperature. The weight change was determined between the weights before and after oxidation testing divided by the initial sample surface area.

Oxidation testing of the SMRT and coarse grain (CG) samples was carried out in a stagnant liquid LBE alloy (45Pb-55Bi, in at.%) filled in a quartz container at 550 °C for several durations. The liquid LBE alloy was oxygen-saturated. A lead oxide layer covered the melt surface during oxidation measurements. The detailed test procedure in LBE can be found in Ref. [15].

Structure, Composition and Phase Characterizations

Weight changes of samples before and after high-temperature exposures were measured by an electric balance with 0.01 mg accuracy. Cross-sectional morphologies of the oxidized samples in air and in liquid LBE alloy were observed using a scanning electron microscope (SEM) on an FEI Nova Nansen 430 instrument. Compositional distributions in the surface layer were monitored by an electron probe microanalyzer (EPMA) on a Shimadzu EPMA-1610 system. In addition, X-ray diffraction (XRD) analyses were carried out to identify the phase constituents in the oxide scale, by a Rigaku D/max 2400 X-ray diffractometer (12 kW) with Cu K_α radiation and a step size of 0.02°. The elemental binding states of oxides were studied by X-ray photoelectron spectroscopy (XPS) on a Thermo Scientific ESCALAB 250 system, with Al $K_{\alpha 1}$ radiation and an Ar ion gun of 3 kV × 2 μA for sputtering.

Results and Discussion

Oxidation Behavior in Air

The microstructure of SMRT 9Cr2WVTa sample has been reported in detail in Ref. [15]. A gradient nanostructure was fabricated on the surface layer of the 9Cr2WVTa and 9Cr+AlSi steels: The thickness of plastic deformation was ~ 80 μm, and the grain size of top surface layer was ~ 50 nm. Figure 1 shows the microstructure of the SMRT 9Cr2WVTa sample. A gradient nanostructured surface layer in SMRT 9Cr2WVTa was present, as shown by the cross-sectional SEM morphology in Fig. 1. The nanosized grains at the top surface layer are nearly equiaxed with an average size of ~ 30 nm, as shown in Fig. 1b and c. The average grain size at a distance of 30 μm beneath the surface is 80 nm (Fig. 1d, e). The matrix microstructure was found to consist of lath martensite, as shown in Fig. 1f, g.

Figure 2 shows plots of the weight versus oxidation time of the SMRT and the coarse grain (CG) 9Cr2WVTa and 9Cr+AlSi samples at 700 °C in air for 500 h. It can be seen that there are two distinct stages in the weight gain curves of SMRT and CG 9Cr2WVTa steel. Before 80 h, the weight values were similar and grew slowly, which is the first stage. After 80 h, it came to the second stage with a rapid rate of oxidation. The weight of 9Cr+AlSi steel was much lower than that of 9Cr2WVTa steel. For example, the mean weight of CG 9Cr+AlSi sample is ~ 0.088 μg mm^{-2} after oxidation for 500 h, less than that for CG 9Cr2WVTa sample (~ 0.478 μg mm^{-2}). Moreover, the weight gain per unit area of the SMRT sample increased slower than that of the CG sample, especially for the 9Cr+AlSi steel. The mean weight gain for the SMRT 9Cr+AlSi sample is ~ 0.024 μg mm^{-2} after oxidation for 500 h, about one-fourth of that for the CG 9Cr+AlSi sample (~ 0.088 μg mm^{-2}).

Phase analyses on oxide by XRD on 9Cr2WVTa and 9Cr+AlSi samples after oxidation at 700 °C for 500 h are shown in Fig. 3. The oxide products on the SMRT and CG 9Cr2WVTa samples were mostly composed of Fe_2O_3 after oxidation in air at 700 °C for 500 h, as shown in Fig. 3a, b. The oxide scale formed on CG 9Cr+AlSi steel was the same as that of 9Cr2WVTa steel in Fig. 3d. Cr_2O_3 and $CrMn_{1.5}O_4$ were formed on the SMRT 9Cr+AlSi sample after the same oxidation treatment, as shown in Fig. 3c. Peaks of α-Fe were on XRD pattern for SMRT 9Cr+AlSi sample, which indicates that the oxide formed on SMRT 9Cr+AlSi was much thinner than that on CG 9Cr+AlSi steel.

Figure 4 shows SEM images of the surface oxide formed on 9Cr2WVTa and 9Cr+AlSi steels after exposure in air at 700 °C for 500 h. The microstructure of the

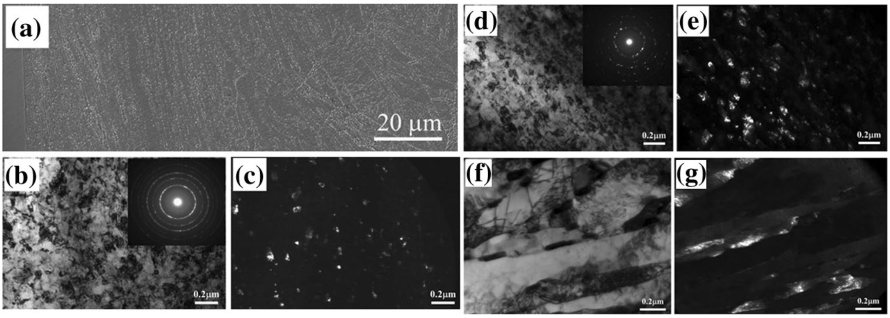

Fig. 1 Microstructure of SMRT 9Cr2WVTa sample **a** cross-sectional SEM images, **b** bright-field and **c** dark-field TEM images of the top surface layer, **d** bright-field and **e** dark-field TEM images at a distance of 30 μm beneath surface, **f** bright-field and **g** dark-field TEM images of matrix metal

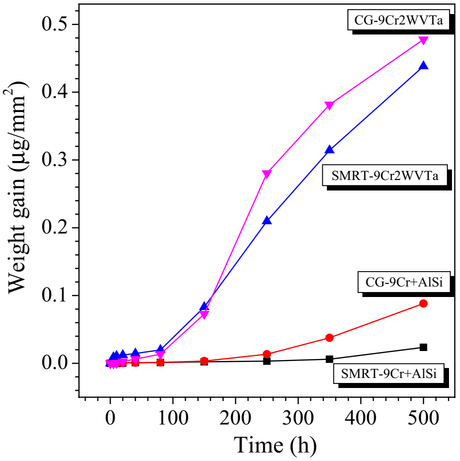

Fig. 2 Specific weight gains measured as a function of oxidation time up to 510 h at 700 °C in air for the SMRT and CG 9Cr2WVTa and 9Cr+AlSi samples

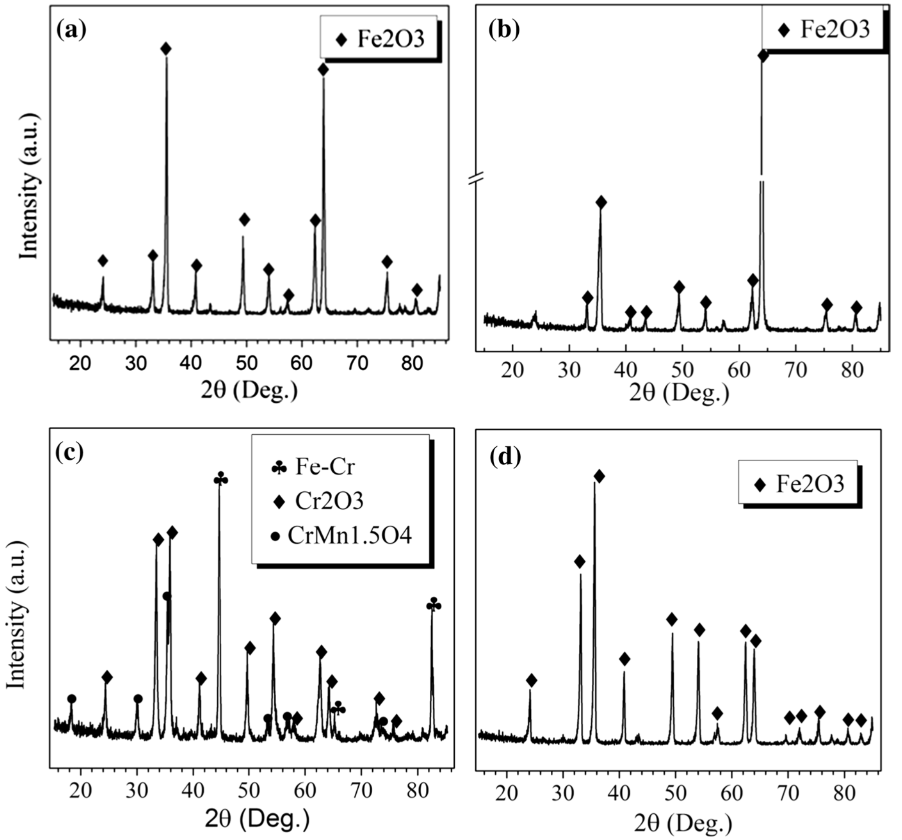

Fig. 3 XRD patterns of SMRT (**a**), CG (**b**) 9Cr2WVTa sample and SMRT (**c**), CG (**d**) 9Cr+AlSi sample after oxidation at 700 °C for 500 h in air

oxides formed on 9Cr2WVTa and 9Cr+AlSi steels is different. The SEM+EDS and XRD results show that the loose and porous needle-like Fe_2O_3 oxides formed on 9Cr2WVTa steel, as shown in Fig. 4a, b. The granular oxides formed on the surface of the 9Cr+AlSi steel are Cr- and Mn-rich and compact, as shown in Fig. 4c, d.

SEM images of oxide layer on 9Cr2WVTa and 9Cr+AlSi specimens exposed at 700 °C for 500 h are shown in Fig. 5. The oxide layer thickness on SMRT 9Cr2WVTa was smaller than that on CG 9Cr2WVTa, which is 112 and 150 μm, respectively. The element distributions in the oxide scale on 9Cr2WVTa and 9Cr+AlSi steels in air at 700 °C for 500 h are shown in Figs. 6 and 7. The results revealed the double-layer structure in oxidation layer, with outer layer enriched with Fe and O and the inner layer enriched with Fe, Cr and O, as shown in Fig. 6a, b. There are cracks existed in the outer oxide layer, especially in the interface between inner and outer oxide layer. A continuous and compact Cr_2O_3 layer formed on the SMRT 9Cr+AlSi steel, as shown in Fig. 7a. Al and Si are enriched beneath the Cr_2O_3 layer.

The material investigated in the present study is the 9% Cr steel. It has reported that a duplex oxidation layer forms on the surface of 9% Cr steel in air at high temperature, which is composed of the Fe–Cr spinel inner layer and Fe_2O_3 outer layer [16]. For a thick oxide scale, it is difficult to detect all the oxides in a thick oxide scale by XRD, so only Fe_2O_3 was found in the XRD

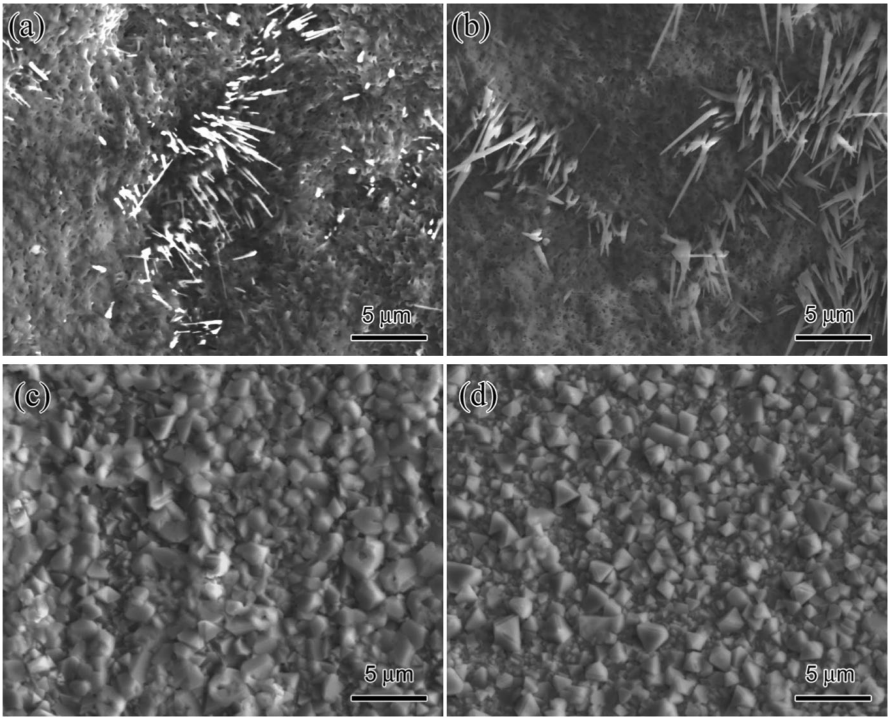

Fig. 4 SEM images of the surface oxide on SMRT (**a**), CG (**b**) 9Cr2WVTa sample and SMRT (**c**), CG (**d**) 9Cr+AlSi sample after oxidation at 700 °C for 500 h in air

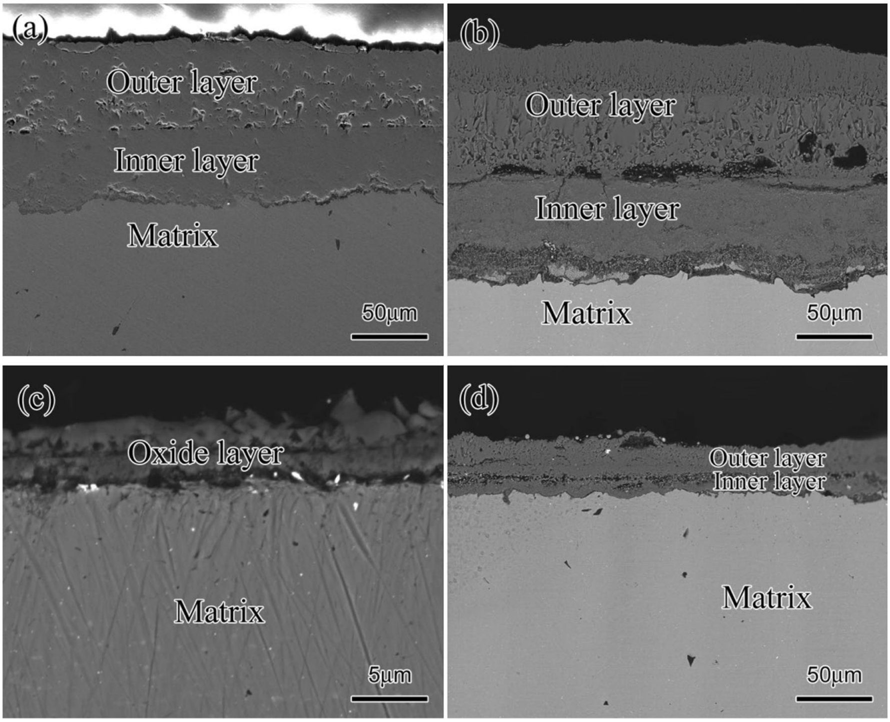

Fig. 5 Cross-sectional SEM morphologies of SMRT (**a**), CG (**b**) 9Cr2WVTa sample and SMRT (**c**), CG (**d**) 9Cr+AlSi sample after oxidation at 700 °C for 500 h in air

spectra as shown in Fig. 3a, b, d. But according to the EPMA results, it was deduced that the inner oxide layer consists of the Fe–Cr spinel. So the oxide scale on SMRT and CG 9Cr2WVTa was double layered in structure, consisting of an Fe_2O_3 outer layer and Fe–Cr spinel inner layer as shown in Fig. 5a, b. The inner oxide layer is more compact than the outer layer. Moreover, compared with SMRT 9Cr2WVTa sample, the inner oxide layer of CG 9Cr2WVTa is rather porous and loose and some cracks were found in the inner layer. The microstructure of the oxide layer formed on the CG 9Cr+AlSi steel is the same as that on 9Cr2WVTa. However, the oxide layer thickness is thinner that on CG 9Cr2WVTa, about 35 μm, as shown in Fig. 5d. A thin compact oxide scale formed on the SMRT 9Cr+AlSi, which was about 4.5 μm, as shown in Fig. 5c.

The outmost region of the oxide scale on the SMRT 9Cr+AlSi sample after oxidation at 700 °C for 500 h in air was enriched in both Mn and Cr, as shown in Fig. 8. To verify the existence of Al_2O_3 and SiO_2, the elemental binding states and depth distributions were monitored by XPS. The peaks of Al and Si oxides were found in a full XPS spectrum of oxide layer, as shown in Fig. 9. The outer oxide layer of CG 9Cr+AlSi steel consists of Fe oxides. The inner oxide layer consisted of Fe, Cr, Mn, O, Al and Si, as shown in Fig. 7b.

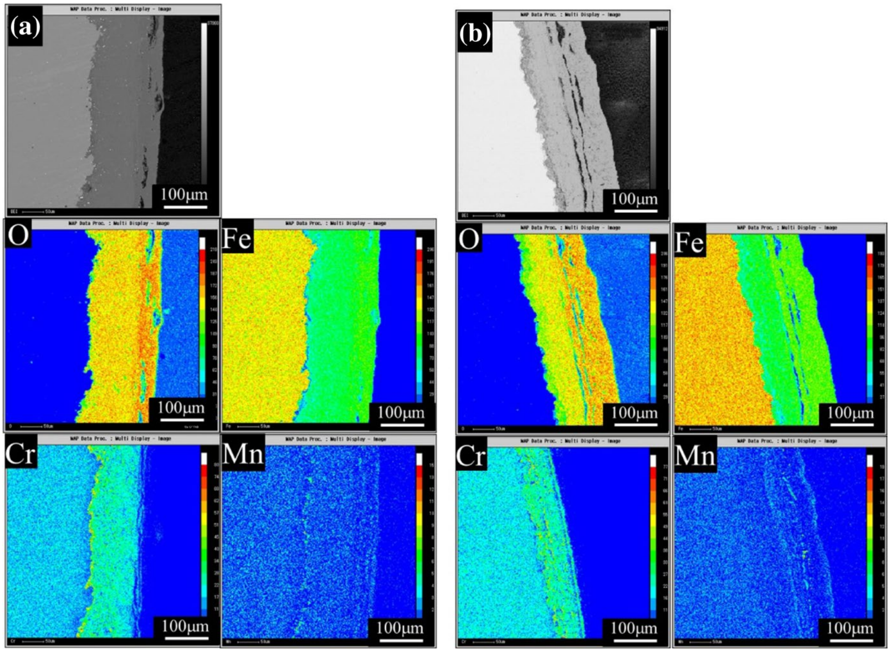

Fig. 6 EPMA images of oxide scale on **a** the SMRT 9Cr2WVTa sample and **b** the CG 9Cr2WVTa sample after oxidation at 700 °C for 500 h in air

Oxidation Mechanism

The Oxidation Mechanism of 9Cr2WVTa and 9Cr+AlSi

The addition of Al and Si reduced the oxidation rate of CG 9Cr+AlSi effectively, and the Al- and Si-rich oxides formed in the oxide inner layer. The nanostructured surface layer fabricated on the surface of SMRT 9Cr+AlSi enhanced the oxidation resistance significantly, due to a compact and Al-, Cr- and Si-enriched single oxide layer formed on the surface of SMRT 9Cr+AlSi. But the nanostructured surface layer had less effect on the oxidation resistance of 9Cr2WVTa sample at 700 °C and a duplex oxide layer had formed, which consisted of an Fe-enriched external oxide layer and an Fe–Cr spinel oxide inner layer.

It has been demonstrated that Al has marked effects on the oxidation resistance characteristic of Fe–10Cr [17]. Approximately 8–12% aluminum is required for α-A1203 formation on binary M–A1 alloys, where M = Ni, Co or Fe [18]. But a lower concentration of aluminum is needed to establish an A1203 layer if chromium is present in the alloy [19]. Wagner proposed that chromium acts as an oxygen getter by forming a Cr_2O_3 scale, thus reducing the activity of oxygen at the alloy–scale interface to the extent that the internal oxidation of aluminum is prevented [20, 21]. According to Guan and Smeltzer [22], the effect of chromium in Ni–Cr–A1 alloys is attributable to thermodynamic interactions, with chromium both reducing the solubility of oxygen in the alloy and altering the concentration

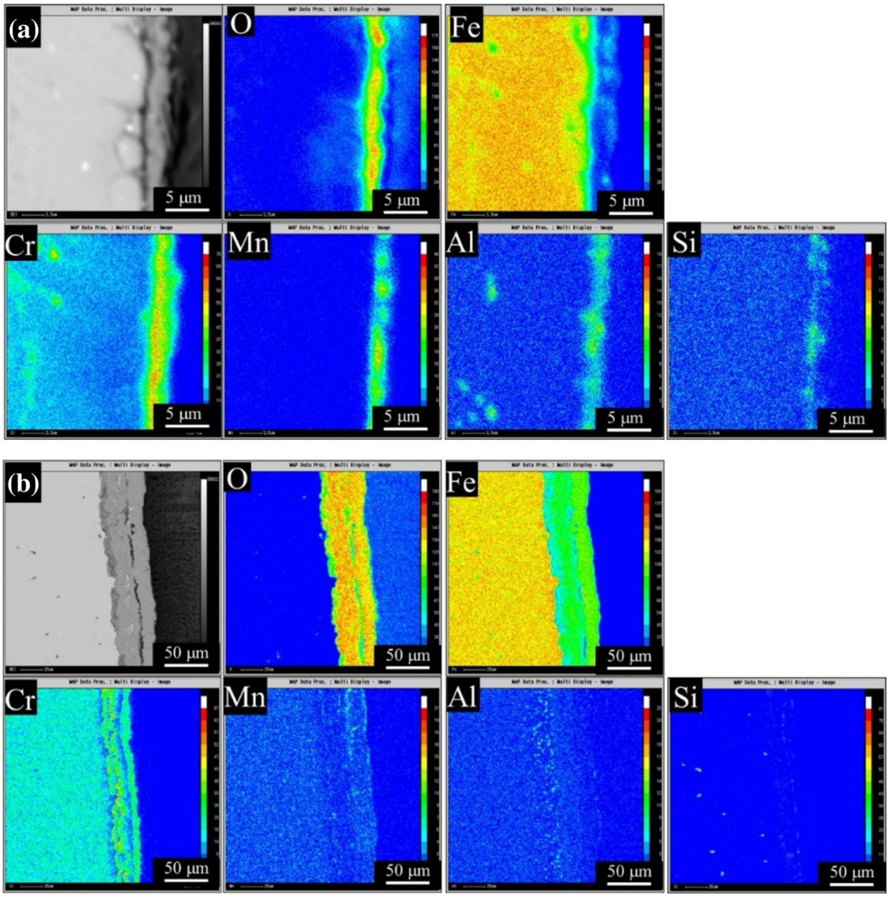

Fig. 7 EPMA images of oxide scale on **a** the SMRT 9Cr+AlSi sample and **b** the CG 9Cr+AlSi sample after oxidation at 700 °C for 500 h in air

profiles in the alloy subsurface to the extent that oxygen supersaturation necessary for the onset of internal oxidation is avoided.

A low silicon content of 0.05–1.0% might or might not be sufficient to form a continuous SiO_2 layer at the alloy–scale interface, but is sufficient to have a beneficial effect on oxidation kinetics, particularly by facilitating exclusive Cr203 scale formation [23–26].

It has been proposed that when Si is added to Fe–Cr alloys, a relatively small amount of silicon is required to form a continuous layer of silica beneath the chromia scale [27, 28]. Jones and Stringer showed that the oxidation mode for the Co-25Cr alloy changes from the development of a fast-growing duplex structure to the formation of a protective Cr_2O_3 scale with the presence of as little as 0.05% silicon in the alloy [29].

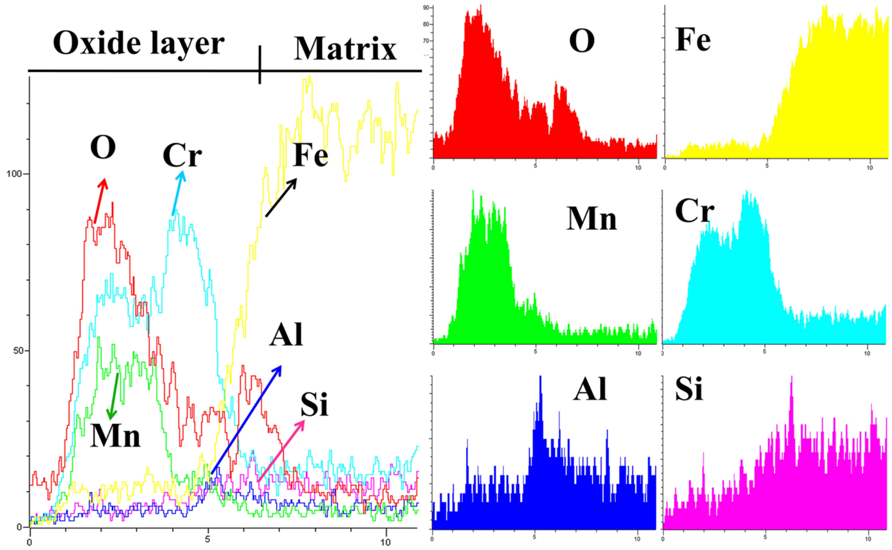

Fig. 8 The EDS line-scanning diagram across the oxide scale on the SMRT 9Cr+AlSi sample after oxidation at 700 °C for 500 h in air

Gulbransen and Andrew reported that the beneficial effects of addition of silicon to a Ni-20 Cr alloy are optimized if the silicon content is kept low (0.25%) and a small amount of manganese (0.05%) is added [30].

Mn is inclined to replace Cr to form Mn_2O_3 (for low fraction of Mn) or form Mn–Cr spinel (for high fraction of Mn) [31]. For instance, a Mn-enriched oxide layer instead of a Cr-enriched one formed on the surface of SMRT 9Cr2WVTa sample after oxidation in air at 600 °C [32]. Nanocrystallization has been demonstrated as an alternative approach to increase the preferential or selective oxidation ability of alloy [33]. It was suggested that reducing grain size will improve the diffusion rate of atoms and increase the nucleation site of oxides [34].

Hence, the good resistance to oxidation of SMRT 9Cr+AlSi is due to the high diffusion coefficient of alloy elements in the nanostructure and the existence of 9 wt.% Cr in the base metal. The selective oxidation of Cr, Al and Si was accelerated to form the protective Al_2O_3 and SiO_2 layer, which are effective barriers to stop the transport of oxygen and metal cations. For SMRT 9Cr2WVTa, although the diffusion rate of Cr is enhanced by the nanostructure, the content of Cr is not enough to promote the selective oxidation of Cr in SMRT 9Cr2WVTa, so that a duplex oxide layer formed. Although the amount of Al and Si added to the CG 9Cr+AlSi alloy appeared to be insufficient to form a continuous silica layer under the present experimental conditions, the growth rate of the oxide scale still decreased.

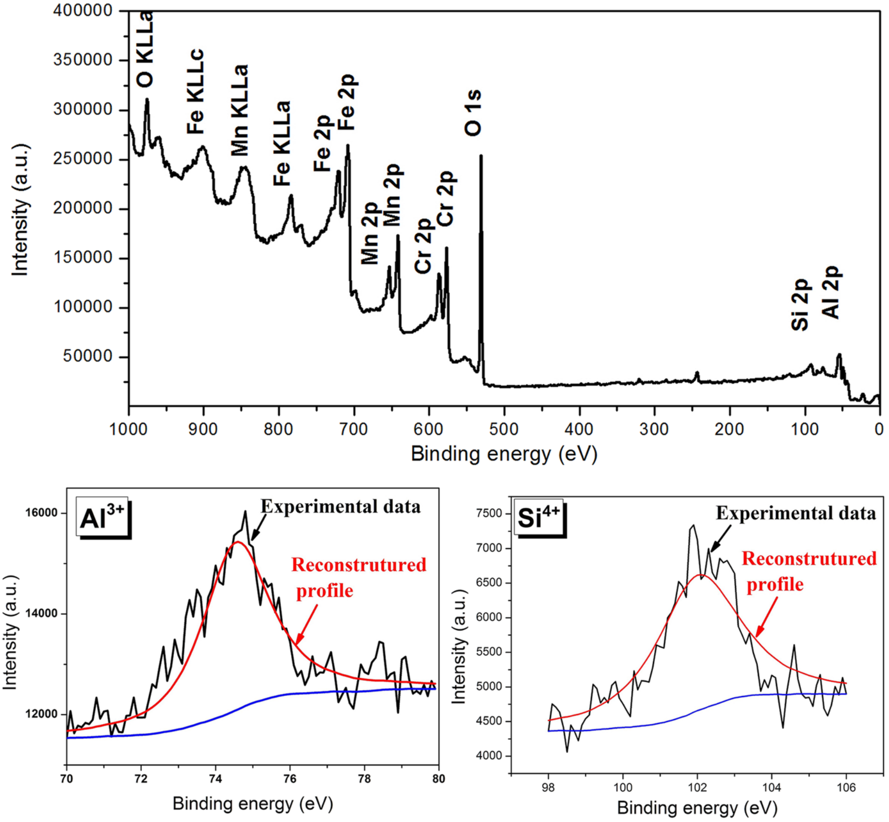

Fig. 9 A full XPS spectrum and curve fitting of Al 2p and Si 2p components by using Al3+ and Si4+ signal of the oxide scale on the SMRT 9Cr+AlSi sample after oxidation at 700 °C for 500 h in air

The Schematic Diagram of Oxidation Mechanism

The alloys researched above can be divided into two groups according to the oxidation mechanism. The oxide scale on the SMRT 9Cr2WVT, CG 9Cr2WVTa and CG 9Cr+AlSi alloy failed to stimulate the selective oxidation, as shown in Fig. 10. Due to the insufficient Cr concentration in SMRT and CG 9Cr2WVTa steels, a mixture of Fe_2O_3 and Cr_2O_3 oxides nucleated on the surface at the initial oxidation stage. The alloy grain boundaries, with high diffusivity paths, supply sufficient Cr to form Cr_2O_3 oxides. However, the flux of Cr in regions away from the grain boundaries depends on much slower bulk diffusion. The Cr flux might not be sufficient to form a continuous chromia layer. Therefore, iron oxides formed in these regions. After prolonged exposure, the rapid outward growth of Fe_2O_3 oxide layer formed a continuous layer, while the inner transportation of oxygen enhanced the inner oxidation of Cr in the matrix. At the final stage, a duplex oxide layer formed which consist of Fe_2O_3 outer layer and Fe–Cr spinel inner layer. Al and Si added in the CG 9Cr+AlSi alloy were insufficient

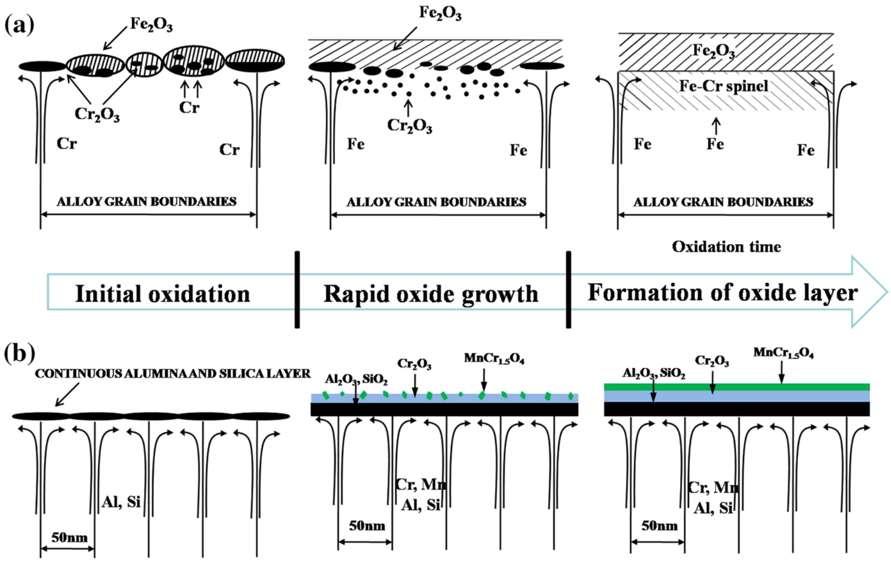

Fig. 10 Schematic representation showing the formation of oxidation mechanism

to form continuous Al_2O_3 and SiO_2 layer, which due to the oxide mechanism of CG 9Cr+AlSi alloy is similar to that of SMRT 9Cr2WVT, CG 9Cr2WVT alloys.

The oxidation schematic diagram of SMRT 9Cr+AlSi alloy is shown in Fig. 10b. Due to the nanostructure obtainable by SMRT, the density of alloy grain boundaries is larger, as shown in Fig. 10b. The higher diffusion coefficient of Al and Si in nanostructure and the increase in driving force by Cr accelerate the selective oxidation of Al and Si. Al and Si diffuse quickly through the grain boundaries to form a continuous alumina and silica layer which lead to undercut any faster-growing transient oxides. Alumina and silica act as a diffusion barrier, decrease the diffusion of alloy elements and oxygen and reduce the high-temperature oxidation rate. Cr and Mn diffuse through the alumina and silica layer to the form of the outer chromia layer and Mn–Cr spinel.

Oxidation Behavior in LBE Melts

The cross-sectional morphologies of different samples after immersion in the liquid 45Pb-55Bi alloy at 550 °C for 500 and 3000 h are shown in Fig. 11. A duplex structure was presented, with an outer magnetite layer and an internal Fe–Cr spinel layer. Pb penetration was observed in the outer oxide layer. Oxide diffusion zone (ODZ) was formed beneath the inner oxide layer. The thickness of oxide layer on CG 9Cr+AlSi after 500-h and 3000-h oxidation was 10.0 and 28.2 μm, respectively, as shown in Fig. 11b, e. That on SMRT 9Cr+AlSi was thinner, 8.8 and 24.3 μm, respectively, as shown in Fig. 11c, f. The oxide layer of SMRT and CG 9Cr+AlSi is thinner than that of CG 9Cr2WVTa, with the thickness value of about 17.2 and 37.6 μm after 500 and 3000 h, as shown in Fig. 8a, d.

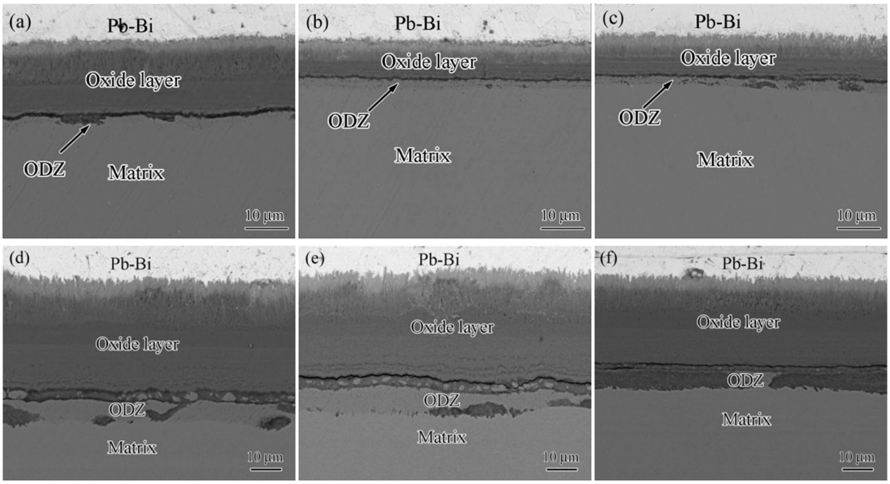

Fig. 11 Cross-sectional SEM images of (**a**, **d**) the CG 9Cr2WVTa, (**b**, **e**) the CG 9Cr+AlSi and (**c**, **f**) the SMRT 9Cr+AlSi samples after immersion in oxygen-saturated LBE melt at 550 °C for 500 h (**a**–**c**) and 3000 h (**d**–**f**)

Fig. 12 Thickness of oxide scale on the CG 9Cr2WVTa, CG and SMRT 9Cr+AlSi samples with immersion time in LBE melt at 550 °C. At least 5 different regions as shown in Fig. 10 have been observed to derive the average value and error bar of the scale thickness on each sample

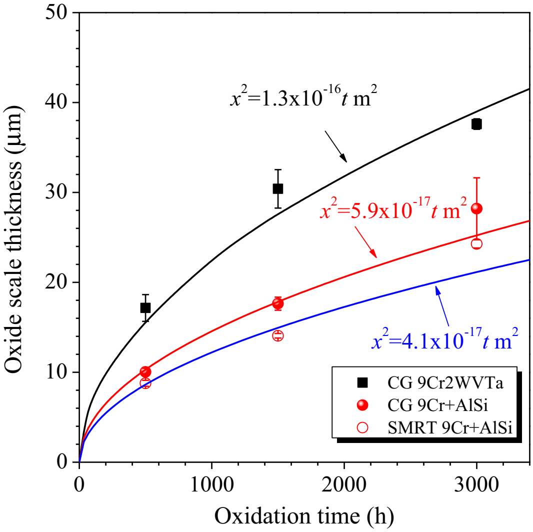

Figure 12 shows the oxide scale thickness gain of different samples exposed to LBE for different times at 550 °C. A parabolic law ($h^2 = K_p t$) fits the experimental kinetics of the oxide scale growth. The experimental parabolic rate constant K_p of CG 9Cr2WVTa is ~ 1.3×10^{-16} m^2 s^{-1} [35]. The values of SMRT and CG 9Cr+AlSi were estimated to be ~ 4.1×10^{-17} m^2 s^{-1} and ~ 5.9×10^{-17} m^2 s^{-1}, respectively. The results show that oxide layer in CG 9Cr+AlSi grows slower than that in CG 9Cr2WVTa and the oxidation rate of SMRT 9Cr+AlSi is slowest.

The additions of Al and Si to 9Cr2WVTa reduced the thickness of oxide layer effectively, which is due to the formation of Al and Si oxides in the internal oxide

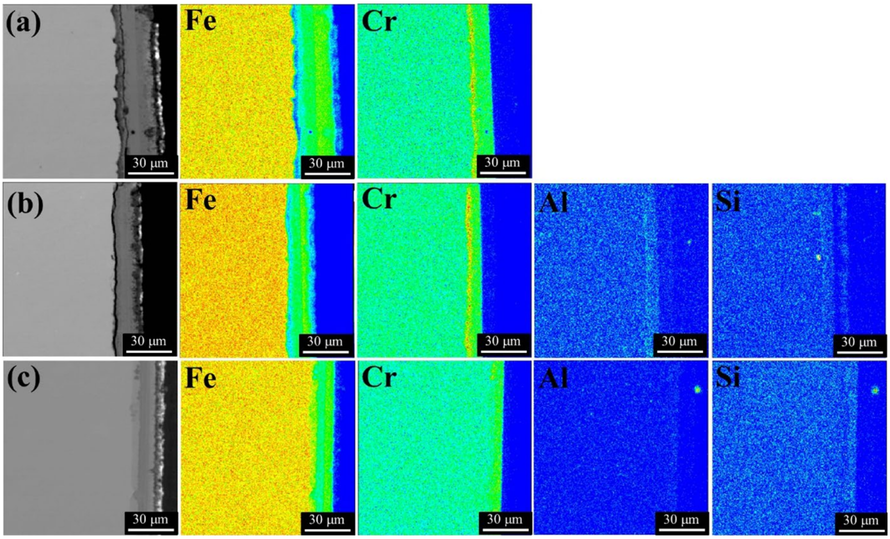

Fig. 13 In-depth composition distributions in the **a** CG 9Cr2WVTa, **b** the CG 9Cr+AlSi, **c** the SMRT 9Cr+AlSi samples immersed in oxygen-saturated LBE melt at 550 °C for 1500 h, measured by EPMA

layer, as shown in Fig. 13. According to the elemental distributions of CG 9Cr+AlSi after tested for 1500 h, enrichment of Cr, Al and Si in the internal oxide layer is clear, as shown in Fig. 13b, while only Cr was enriched in the internal oxide layer of CG 9Cr2WVTa (Fig. 13a). It is demonstrated that the addition of Al is an effective method to improve corrosion resistance of 16 wt.% Cr-ODS steel in LBE and the Si addition to T91 steel likely plays the same role [36]. The presence of Si in EP823 Russian steel promotes the formation of silicon-enriched oxides in the internal oxide layer leading to lower oxide layer growth, which improves the resistance to oxidation [36]. Because the growth rates of the external and internal oxide layer were controlled, respectively, by the Fe diffusion rate in oxide layer and the oxygen transportation rate in nanochannels, the nanostructured surface layer in the SMRT 9Cr2WVTa failed to enhance the oxidation resistance effectively. Nanostructured layer in T91 steel has little effect on the oxidation resistance in LBE and also conforms to the oxidation mechanism [36].

However, the nanostructured layer reduced the oxide rate of SMRT 9Cr+AlSi with a certain degree, which is due to the diffusion of Al and Si into the internal oxide layer promoted by the nanostructured layer, as shown in Fig. 13c. The nanostructured layer has the same effect on Fe-13Cr steel with adding Al and Si, which enhanced the oxidation resistance in LBE [36].

Conclusions

The oxidation resistance of the SMRT 9Cr2WVTa sample was faintly enhanced at 700 °C in air. A duplex oxide scale was formed, which is composed of a loose outer Fe_2O_3 layer and a compact Fe–Cr spinel oxide layer.

The selective oxidation was accelerated on the SMRT 9Cr+AlSi sample, which was due to the enhancement of diffusion coefficient of Al and Si in nanostructure and the increase in driving force Al and Si by Cr. Al and Si were selective oxidized to form continuous and compact alumina and silica layer. Then, the outer diffusion of Cr and Mn formed the homogeneous Cr_2O_3 layer as well as $CrMn_{1.5}O_4$ particles. The growth is described by a parabolic law, and the parabolic rate constant Kp of SMRT and CG 9Cr+AlSi was 4.1×10^{-17} m^2 s^{-1} and 5.9×10^{-17} m^2 s^{-1}, respectively. The oxidation resistance decreases in the sequence: SMRT 9Cr+AlSi, CG 9Cr+AlSi, SMRT 9Cr2WVTa, CG 9Cr2WVTa. The Al and Si in the 9Cr+AlSi improved the oxidation resistance in liquid LBE alloy. The nanostructured layer in SMRT 9Cr+AlSi enhanced the diffusion rates of Al and Si into internal oxide layer and promoted the formation of protective oxide scales.

Acknowledgements This work was financially supported by the Major Research Plan of the National Natural Science Foundation of China (No. 91226204) and the Strategic Priority Research Program of the Chinese Academy of Science (No. XDA03010304).

References

1. R. Klueh and A. Nelson, *Journal of Nuclear Materials* **371**, (1), 2007 (37–52).
2. H. Tanigawa, K. Shiba, H. Sakasegawa, T. Hirose and S. Jitsukawa, *Fusion Engineering and Design* **86**, (9), 2011 (2549–2552).
3. A. Kohyama, Y. Kohno, K. Asakura and H. Kayano, *Journal of Nuclear Materials* **212**, 1994 (684–689).
4. N. Baluc, R. Schäublin, P. Spätig and M. Victoria, *Nuclear Fusion* **44**, (1), 2004 (56).
5. G. Butterworth, *Journal of Nuclear Materials* **179**, 1991 (135–142).
6. R. Klueh and E. Bloom, *Nuclear Engineering and Design. Fusion* **2**, (3), 1985 (383–389).
7. D. Dulieu, K. Tupholme and G. Butterworth, *Journal of Nuclear Materials* **141**, 1986 (1097–1101).
8. M. Tamura, H. Hayakawa, M. Tanimura, A. Hishinuma and T. Kondo, *Journal of Nuclear Materials* **141**, 1986 (1067–1073).
9. T. Noda, F. Abe, H. Araki and M. Okada, *Journal of Nuclear Materials* **141**, 1986 (1102–1106).
10. Z. Lu, R. Faulkner, N. Riddle, F. Martino and K. Yang, *Journal of Nuclear Materials* **386**, 2009 (445–448).
11. H. Qun-ying, L. Chun-jing, L. Yan-fen, L. Shao-jun, W. Yi-can, L. Jian-gang, W. Fa-rong, J. Xin, S. Yi-yin and Y. Jin-nan, *Chinese Journal of Nuclear Science and Engineering* **1**, 2007 (008).
12. J. S. Dunning, D. E. Alman and J. C. Rawers, *Oxidation of Metals* **57**, (5), 2002 (409–425).
13. T. Ishitsuka, Y. Inoue and H. Ogawa, *Oxidation of Metals* **61**, (1), 2004 (125–142).
14. S. G. Wang, M. Sun, H. B. Han, K. Long and Z. D. Zhang, *Corrosion Science* **72**, 2013 (64–72).
15. R. L. Klueh and D. R. Harries, *High-Chromium Ferritic and Martensitic Steels for Nuclear Applications*, (ASTM, West Conshohocken, 2001).
16. N. Birks, G. H. Meier and F. S. Pettit, *Introduction to the High-Temperature Oxidation of Metals*, (Cambridge University Press, New York, 2006), p. 131.
17. S. Sadique, A. Mollah, M. Islam, M. Ali, M. Megat and S. Basri, *Oxidation of Metals* **54**, (5–6), 2000 (385–400).
18. F. H. Stott, in *Materials Science Forum*, Vol. 251 (Trans Tech Publications, 1997), pp. 19–32.
19. F. H. Stott and G. C. Wood, *Oxidation of Metals* **44**, 1995 (113–145).
20. C. S. Giggins and F. S. Pettit, *Journal of the Electrochemical Society* **118**, (11), 1971 (1782–1790).
21. G. N. Irving, J. Stringer and D. P. Whittle, *Corrosion* **33**, 1977 (56–60).
22. S. W. Guan and W. W. Smeltzer, *Oxidation of Metals* **42**, 1994 (375).
23. J. F. Radavich, *Corrosion* **15**, 1959 (613–617).
24. D. E. Jones and J. Stringer, *Oxidation of Metals* **9**, 1975 (409).
25. F. H. Stott, G. J. Gabriel, F. I. Wei and G. C. Wood, *Materials and Corrosion* **38**, (9), 1987 (521–531).
26. B. Gleeson and M. A. Harper, *Oxidation of Metals* **49**, (3–4), 1998 (373–399).

27. G. H. Meier, K. Jung, N. Mu, N. M. Yanar, F. S. Pettit, J. P. Abellán, T. Olszewski, L. N. Hierro, W. J. Quadakkers and G. R. Holcomb, *Oxidation of Metals* **74**, (5–6), 2010 (319–340).
28. L. Mikkelsen, S. Linderoth, J. Bilde-Sørensen, in Materials Science Forum, (Trans Tech Publ, 2004), p. 117.
29. DE Jones and J. Stringer, *Oxidation of Metals* **9**, (5), 1975 (409–413).
30. E. A. Gulbransen and K. F. Andrew, *Journal of the Electrochemical Society* **106**, (11), 1959 (941–948).
31. G. R. Holcomb and D. E. Alman, *Scripta Materialia* **54**, (10), 2006 (1821–1825).
32. Y. H. Lu, Z. B. Wang, Y. Y. Song and L. J. Rong, *Corrosion Science* **102**, 2016 (301–309).
33. X. Peng, *Nanoscale* **2**, 2010 (262–268).
34. F. H. Wang, *Oxidation of Metals* **48**, 1997 (215–224).
35. F. Stott, G. Gabriel, F. Wei and G. Wood, *Materials and Corrosion* **38**, (9), 1987 (521–531).
36. B. Gleeson and M. Harper, *Lifetime Modelling of High Temperature Corrosion Processes:(EFC 34)*, (Maney Publishing, London, 2001), p. 167.

Affiliations

Yanhong Lu[1] · Maolong Zhang[1] · Weibao Tang[1] · Yuanyuan Song[2] · Lijian Rong[2]

✉ Lijian Rong
ljrong@imr.ac.cn

[1] Shanghai Electric Nuclear Power Equipment Co., Ltd, Shanghai 201306, China

[2] Key Laboratory of Nuclear Materials and Safety Assessment, Institute of Metal Research,
Chinese Academy of Sciences, Shenyang 110016, China